Enhanced carbon dioxide electroreduction to carbon monoxide over defect rich plasma-activated silver catalysts

Hemma Mistry,[1,2] Yong-Wook Choi,[1] Alexander Bagger,[3] Fabian Scholten,[1] Cecile Bonifacio,[4] Ilya Sinev,[1] Nuria J. Divins,[1] Ioannis Zegkinoglou,[1] Hyo Sang Jeon,[1] Kim Kisslinger,[5] Eric A. Stach,[5] Judith C. Yang,[4] Jan Rossmeisl,[3*] Beatriz Roldan Cuenya[1,*]

[1]Department of Physics, Ruhr University Bochum, 44780 Bochum, Germany

[2]Department of Physics, University of Central Florida, Orlando, Florida 32816, USA

[3]Department of Chemistry, University of Copenhagen, Copenhagen, Denmark

[4]Chemical and Petroleum Engineering and Physics, University of Pittsburgh, Pittsburgh, Pennsylvania 15261, USA.

[5]Center for Functional Nanomaterials, Brookhaven National Laboratory, Upton, New York 11973, USA.

*e-mail: Beatriz.Roldan@rub.de, jan.rossmeisl@chem.ku.dk

Abstract

Efficient, stable catalysts with high selectivity for a single product are essential to making the electroreduction of CO_2 a viable route to the synthesis of industrial feedstocks and fuels. We reveal how a plasma oxidation pre-treatment can lead to an enhanced content of low-coordinated active sites which dramatically lower the overpotential and increase the activity of CO_2 electroreduction to CO. At -0.6 V vs. RHE, more than 90% Faradaic efficiency towards CO could be achieved on a pre-oxidized silver foil. While transmission electron microscopy and *operando* X-ray absorption spectroscopy showed that oxygen species can survive in the bulk of the catalyst during the reaction, quasi-*in situ* X-ray photoelectron spectroscopy showed that the surface is metallic under reaction conditions. DFT calculations show how the defect-rich surface

of the plasma-oxidized silver foils in the presence of local electric fields results in a drastic decrease in the overpotential for the electroreduction of CO_2.

Main Text

The electroreduction of CO_2 is a promising technology which could provide a means to synthesize alternative hydrocarbon fuels by means of consuming waste emissions.[1] However, efficient, stable, and inexpensive catalysts are still needed to electrochemically reduce CO_2 while suppressing the H_2 evolution (HER) side reaction. While gold catalysts show high activity and selectivity to CO at moderate overpotentials,[2] silver is considerably cheaper, and it can also achieve near to 100% selectivity towards CO at higher overpotential.[3] Nanostructuring the surface is one method which may improve the reactivity of Ag-based catalysts for CO_2 electroreduction.[4] For example, nanoporous silver has been shown to have improved performance in comparison to flat Ag,[4a, 5] possibly due to the enhanced binding of intermediates at low coordinated atomic sites[6] or to mesoscale transport effects.[5b] Ag nanoparticles have also shown increased activity for CO_2 reduction to CO with decreasing particle size down to 5 nm.[4b, 4c] Recent attention has also been paid to metal catalysts including Ag[7] which are pre-oxidized and then reduced *in situ* under CO_2 electroreduction conditions, which show vastly improved reactivity in comparison to unoxidized catalysts.[8] However, the mechanism causing their improved behavior is under debate. A consistent picture is still required which describes the role of subsurface oxygen and cationic metal species versus morphological surface modifications (roughening and nanostructuring) for silver catalysts.

In this study, we used plasma treatments to synthesize oxidized and highly-defective nanostructured silver catalysts for selective CO_2 electroreduction to CO at low overpotential. Advanced *in situ* and *operando* X-ray spectroscopy measurements showed that while oxygen could survive in the bulk of the catalyst during the reaction, the near surface region of the catalyst is metallic. Using density functional theory (DFT) calculations, the enhanced activity could be assigned to the highly undercoordinated surface of the pre-oxidized catalysts, which in the presence of local electric fields can lower the overpotential for CO_2 reduction.

Nanostructured Ag catalysts were synthesized by treating Ag foils in low-pressure plasmas of H_2, Ar, or O_2 gas. Figure 1 and Figure S2 show scanning electron microscopy (SEM)

images of Ag catalysts after surface structuring with the plasma treatments. Ar or H_2 plasma introduces small, pore-like defects 50 – 100 nm in size onto the surface, while O_2 plasma causes significant roughening and dense ~50 nm pores on the Ag foil. O_2 plasma followed by a further H_2 plasma treatment (O_2 + H_2 sample) results in further nanostructuring of the Ag surface. The bottom row of Figure 1 shows the samples after 1 hour of CO_2 electroreduction at -0.6V *vs.* RHE. While only mild changes are apparent in the Ar treated sample, the O_2 treated samples show a drastic increase in surface roughness after the reaction, particularly for the O_2 + H_2 sample. These changes may be related to the rapid growth of Ag oxides during O_2 plasma and their subsequent reduction under reaction conditions. SEM measurements of the pre-oxidized catalysts measured after longer reaction times (3 hours) show that the surface structure continues to change over time, Figure S3.

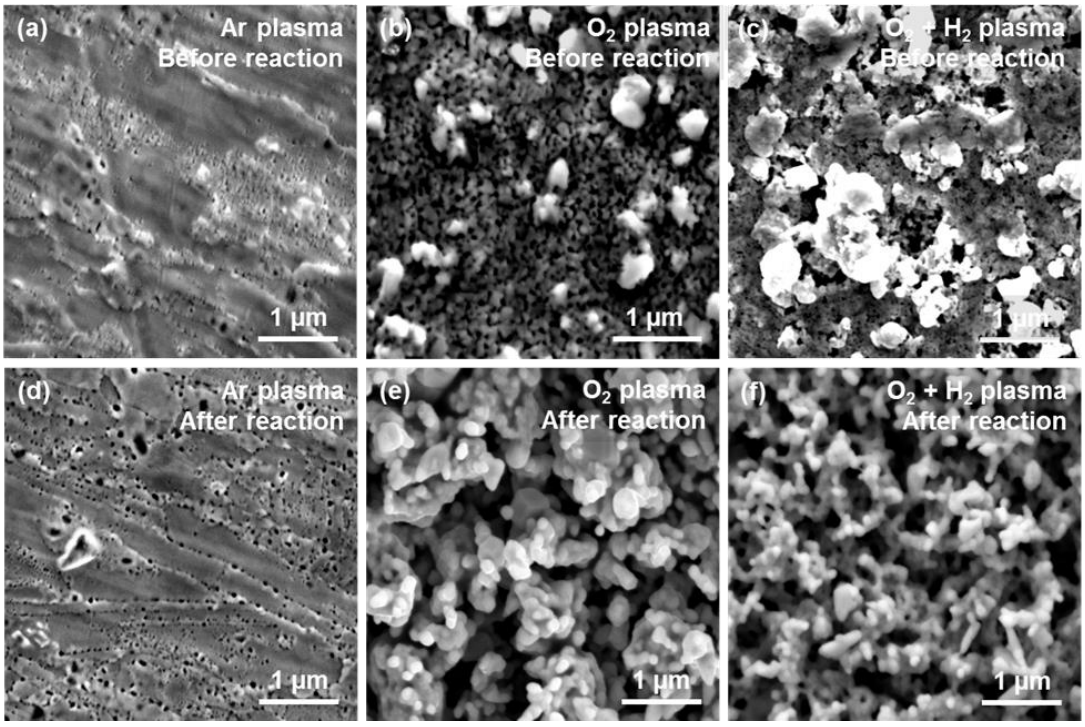

Figure 1. SEM images of plasma treated Ag foils (a-c) as prepared and (d-f) after 1 hour of CO_2 electroreduction at -0.6 V vs. RHE.

Cross-sections of several of the samples were prepared, and scanning transmission electron microscopy – energy dispersive X-ray spectroscopy (STEM-EDS) was measured before and after the reaction in order to gain further insight into the nanostructuring and the changes in

oxidation state of the catalysts caused by the plasma treatments. Figure 2a and b show the Ar plasma treated sample before reaction. Ar plasma causes pore formation not only on the surface, but also below. This pore formation is a result of the plasma treatment, and not an artifact from the sample preparation, as proved by comparison with an untreated Ag sample which shows no pore formation (Figure S4). For the Ar plasma treated sample, the EDS results also indicate only 1 atomic % of O in the top 500 nm of the surface. After the reaction, Figure 2c shows that no major changes occurred to the structure and oxide content of the Ar plasma sample. In comparison, the O_2 plasma treated Ag foil before reaction is very rough and porous and has a high oxygen content. A 35-50 nm thick layer of AgO exists on the surface, while below the surface, Ag grains and regions with ~20% O atom content are present. After 1 hour reaction, the porosity increases, the surface oxide layer has lower oxygen content, and oxygen remains in the bulk of the sample (~6% O). The SEM and STEM images before and after reaction were not measured at identical locations, and so it must be considered that heterogeneities in the sample may in part explain some of the differences before and after reaction. However, we measured several regions within each sample under the different conditions via SEM, and we observed similar structures. Our results indicate that plasma treatment with atomic oxygen can heavily oxidize, roughen, and create defects on an Ag surface, and oxygen can remain in the bulk of these catalysts under the reducing conditions of CO_2 electroreduction.

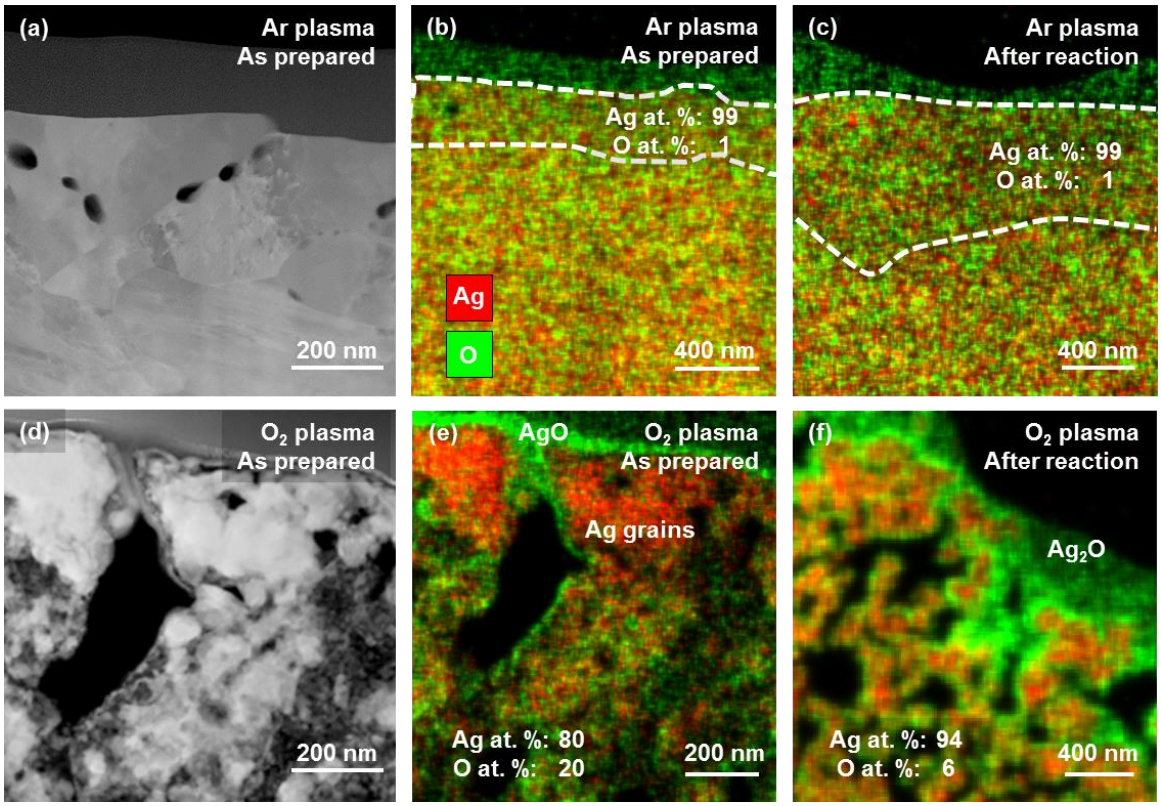

Figure 2. (a, d) SEM and (b-c, e-f) STEM-EDS images of cross-sections of Ag foils treated with (a-c) Ar plasma and (d-f) O_2 plasma, before and after CO_2 electroreduction at -0.6V vs. RHE.

In order to resolve changes in the structure and oxidation state of these catalysts under reaction conditions, we measured extended X-ray absorption fine structure (EXAFS) on the plasma treated Ag catalysts during CO_2 electroreduction. The measurements were performed at a small incidence angle in order to increase the surface sensitivity. In their initial state, the Ar and H_2 plasma treated foils appear similar in EXAFS to an untreated Ag foil, i.e. in their metallic state (Figure S6 and Table S1), while the O_2 and O_2 + H_2 treated samples showed Ag-Ag coordination numbers below 7 and the presence of Ag-O bonds, as shown in Figure 3 and Table S2. The O_2 and the O_2 + H_2 plasma samples were measured *operando* during CO_2 electroreduction for 1 hour at -0.6 V vs. RHE in 0.1 M $KHCO_3$, Figure 3. Impedance measurements were performed to ensure similar electrochemical conditions existed during *operando* measurements as during the lab-based measurements in the standard H-type cell, see Figures S16, S17, and Table S5. During the reaction, the EXAFS results show the reduction of the samples over time. For the O_2 plasma sample, oxides can be detected up to 30 minutes, and

the Ag-Ag coordination number increases to 11 after 65 minutes of reaction. A coordination number lower than 12 may be either due to the extreme roughness and porosity of the sample or due to traces of cationic Ag which remain in the sample but could not be fit in the bulk-sensitive EXAFS data. In comparison, the O_2 + H_2 sample has a lower initial oxygen content, due to the partial reduction with H_2 plasma of the sample surface. In addition, the oxides in this sample reduce more quickly, and the Ag-Ag coordination number increased to 11 after the first 15 minutes. EXAFS of the Ar plasma treated sample was also measured under *operando* CO_2 reduction conditions, however Figure S7 and Table S3 show that it appeared similar in structure to an untreated metallic Ag foil and that no changes could be detected over 30 minutes of reaction.

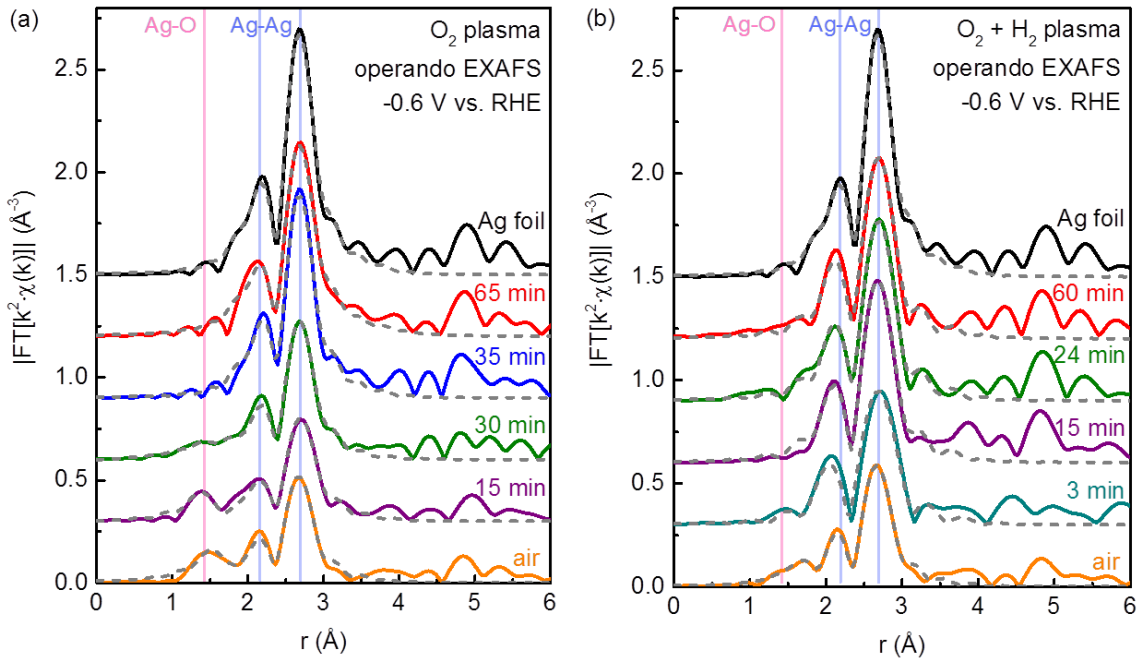

Figure 3. Ag K-edge k^2-weighted EXAFS of (a) O_2 plasma-treated and (b) O_2 + H_2 plasma treated Ag foils measured in air and *operando* during CO_2 electroreduction at -0.6 V vs. RHE. Fits are shown with dashed lines. An untreated Ag foil is plotted for reference.

While the EXAFS and STEM results show the oxidation and structure of the bulk of the samples, characterizing the sample surface under reaction conditions is critical for understanding

its reactivity. To probe the chemical state of the surface of the Ag catalysts during the reaction, quasi-*in situ* X-ray photoelectron spectroscopy (XPS) measurements were performed using an electrochemical cell interfaced to an XPS system, Figure S1. The O_2, O_2 + H_2, and H_2 plasma treated samples were measured with XPS as prepared and after 1 hour of CO_2 electroreduction at -0.6 V vs. RHE, Figure 4a and b. Initially, the H_2 sample contains metallic Ag, with an Ag $3d_{3/2}$ binding energy of 368.3 eV, while the oxidized samples are shifted to lower binding energy of 367.5 eV, characteristic of Ag oxide. After reaction, the Ag 3d spectra for all three samples show only metallic Ag. The Auger regions shown in Figure S5 support these findings. Therefore, despite the survival of oxygen species within the bulk of the sample (EXAFS), the top ~5 nm of the surface probed by XPS are reduced to metallic Ag after 1 hour of reaction.

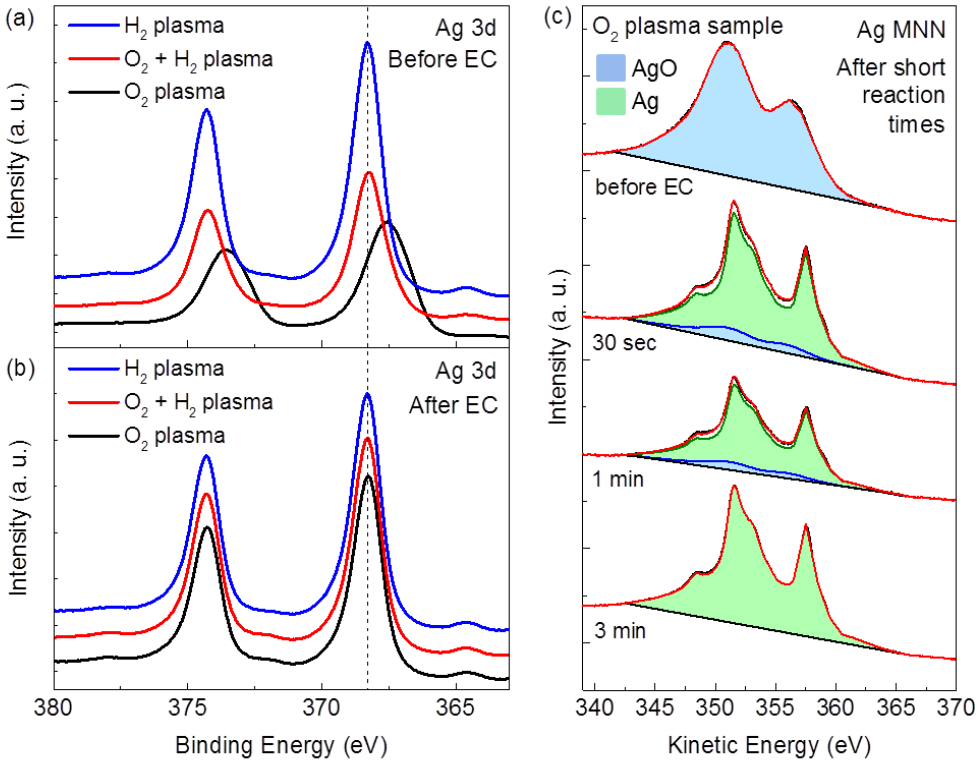

Figure 4. XPS measurements of the Ag 3d region of O_2, H_2 and O_2+H_2 plasma treated Ag catalysts (a) as prepared and (b) after 1 hour of CO_2 electroreduction at -0.6 V *vs*. RHE and UHV transfer to XPS. (c) The Ag MNN Auger region of the O_2 plasma treated sample as prepared and after short reaction times (30 s to 3 min).

In addition to these measurements, XPS data (AES region) after short CO_2 electroreduction reaction times (30 seconds, 1 minute, and 3 minutes at -0.6 V vs RHE) were measured for the O_2 plasma oxidized sample in order to gain insight in how fast the reduction of oxides occurs at the surface, as shown in Figure 4c. The Auger spectra were fit with the line shape of Ag oxide and metallic Ag reference spectra (a Ag foil oxidized for 15 minutes and a Ag(111) single crystal cleaned *in situ*, respectively). After 1 minute of reaction, oxides can still be detected at the surface (~9%), but not after 3 minutes of reaction. This is consistent with the sharp decrease in current observed when starting the reaction (Figure 5a) which corresponds to the initial reduction of silver oxides. Therefore, it is expected that the active site of the reaction for these catalysts under long term operation conditions is metallic Ag.

Figure 5a and b show the current density and Faradaic efficiency towards CO of the plasma treated Ag foils during CO_2 electroreduction at -0.6 V vs. RHE over the course of 3 hours. At this potential, no CO_2 reduction is observed on the H_2 and Ar treated foils, similar to an untreated Ag foil (Figure S8). In contrast, the O_2 and O_2 + H_2 plasma treated samples show exceptional activity and more than 90% selectivity towards CO at this potential. Compared to an untreated Ag foil, the overpotential for CO_2 reduction on plasma-oxidized Ag has been shifted positively by about -0.5 V. Faradaic efficiency towards H_2 is shown in Figure S9.

The efficiency towards CO degrades slightly after three hours of reaction on the oxidized samples, due to a slight decrease in current towards CO and a growth in the HER current, Figure 5c and d. These time-dependent changes are likely related to the change in surface structure over the course of the reaction, as seen in the SEM images (Figure S3). Electrochemical surface roughness measurements also indicate that the roughness of the surface decreases by approximately half between 1 hour and 3 hours of reaction, Figure S10 and Table S4. A decrease in the population of defects over time can therefore be correlated to the slow deactivation of the sample, indicating that sharp nanostructured features present earlier in the reaction may be the key surface sites which enhance CO_2 reduction. It should be noted that the Ar and H_2 plasma samples show higher surface roughness compared to untreated Ag (Table S4), but are still unable to reduce CO_2 at this potential. This means that the improved reactivity of the O_2-plasma treated

samples is not simply due to a surface area increase, but due to the intrinsic ability of the defect sites generated on these samples to reduced CO_2 to CO.

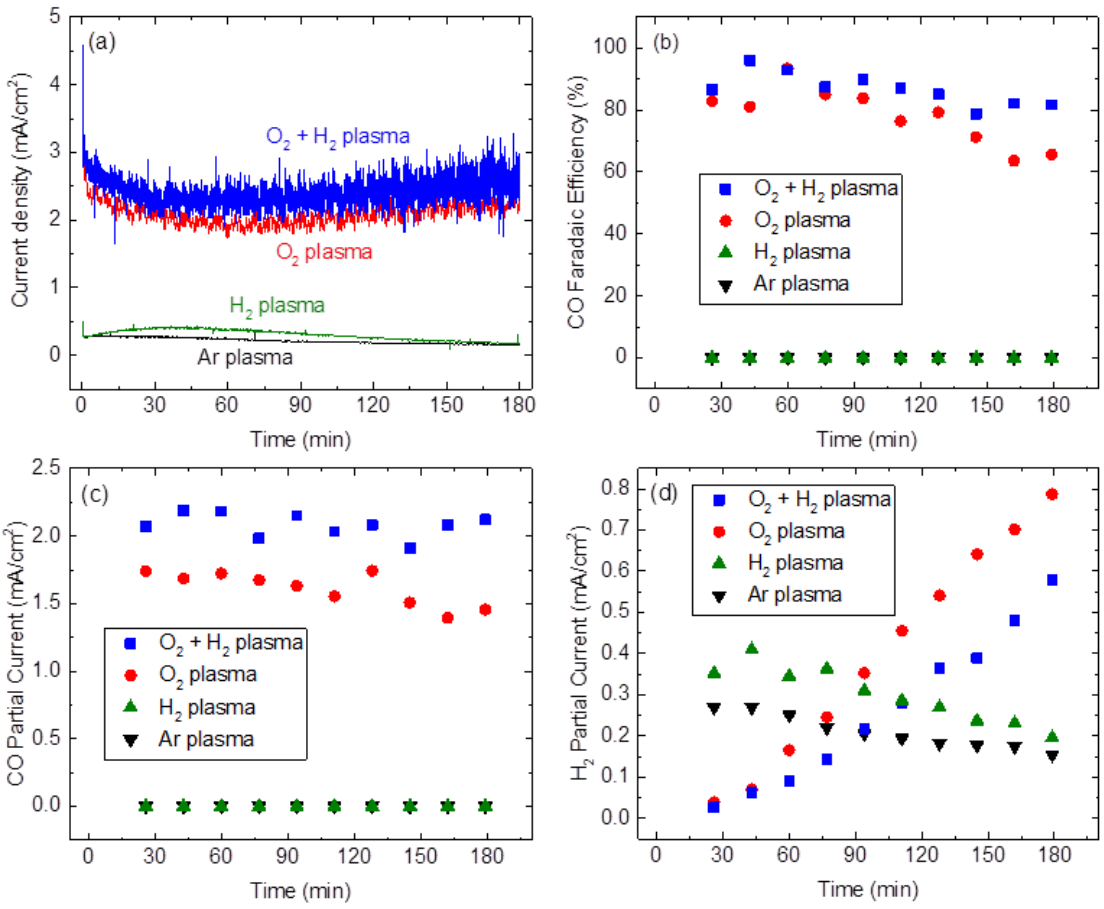

Figure 5. CO_2 electroreduction over plasma-treated Ag foil catalysts at -0.6V vs. RHE in 0.1 M $KHCO_3$. (a) Current density, (b) Faradaic efficiency towards CO, (b) CO partial current, and (d) H_2 partial current.

To understand the effect of the oxygen plasma on the Ag samples, the reaction is studied by DFT. The reactivity is estimated by calculating the free energy differences for the reduction of CO_2 to CO in Figure 6 as a function of the CO binding energy. The volcano-like plot is constructed from multiple models of possible Ag active sites: a 111 facet, 211 step, 111 kink, 211 adatom and 111 adatom (black squares), together with Au and Cu 111 facet and 211 step

(black circles). To construct the volcano-like plot, the overpotential, -ΔG, is determined as the $CO_2 + H^+ + e^- \rightarrow COOH^*$ potential dependent step on the weak binding side, while on the strong binding side, CO* to CO, which is a potential-independent step, is the reaction limiting factor. This enabled us to create the CO_2 reduction volcano, where the weak and strong binding sides of the volcano behave differently with applied potential since they are potential dependent and independent, respectively. Thus, we display the volcano with -0.6 V (red) and with 0 V vs. RHE (blue) potential applied. The potential dependence of the two sides of the volcano is also seen in the top of the volcano, which moves to the right when -0.6 V vs. RHE potential is applied.

The 111 adatom Ag defect has the lowest overpotential to reduce CO_2, at around -0.8 V vs. RHE (See Figure S11 for the free energy diagram). However, the oxygen plasma treated Ag samples can reduce CO_2 at -0.6 V vs. RHE. In order to determine if subsurface oxygen could further lower the overpotential, two structures with subsurface oxygen were investigated, labelled in Figure 6 as "Ag Subsurface Oxygen" (red squares at -0.6 V vs. RHE) and also shown in Figure S12, and S13 for HER. However, as described in more detail in the Supporting Information, the results obtained from these structures deviated strongly from experimental results (e.g. further reduction beyond CO or an increase in HER was predicted but not experimentally observed), making subsurface oxygen an unlikely explanation for the low overpotential CO_2 reduction.

Further investigation of the Ag defect sites shows an increased negative dipole moment for the COOH* adsorbate (see Figure S14), while the CO* adsorbate dipole moment is almost constant. It should be noted that the dipole moment for the adsorbate has been isolated by subtracting the structure dipole moment. The difference in dipole moment of these two adsorbates can be utilized to tune the binding of one while keeping the other constant under the electric field. This is shown in Figure S15, where the presence of a negative electric field enhances the COOH* binding while keeping the CO* binding constant for the Ag 111 adatom and the Ag 111 facet sites. Consistent with the magnitude of the dipole moment, the electric field effect on the Ag 111 adatom is larger than for the Ag 111 facet. Adding the electric field calculations to the volcano plot in Figure 6 (yellow points) shows that the Ag defects allow reduction of CO_2 to CO without further reduction of CO. Because the electric double layer

thickness is around ~ 3 Å, the electric field effect from just the electrode is on the order of -0.2 V/Å.[9] However, pH and solvated ions can enhance the electric field effect up to -1.0 V/Å,[10] and for the Ag 111 adatom defect only an electric field of ~ -0.4 V/Å is required to enable CO_2 reduction. The oxygen plasma treated samples give a highly defective Ag surface which allows reduction of CO_2 at very low overpotentials. Over time, the decrease in surface roughness means that there will be a decrease in the number of defect sites and an increase in terrace-like sites, which will decrease the rate of CO_2 reduction and increase HER.

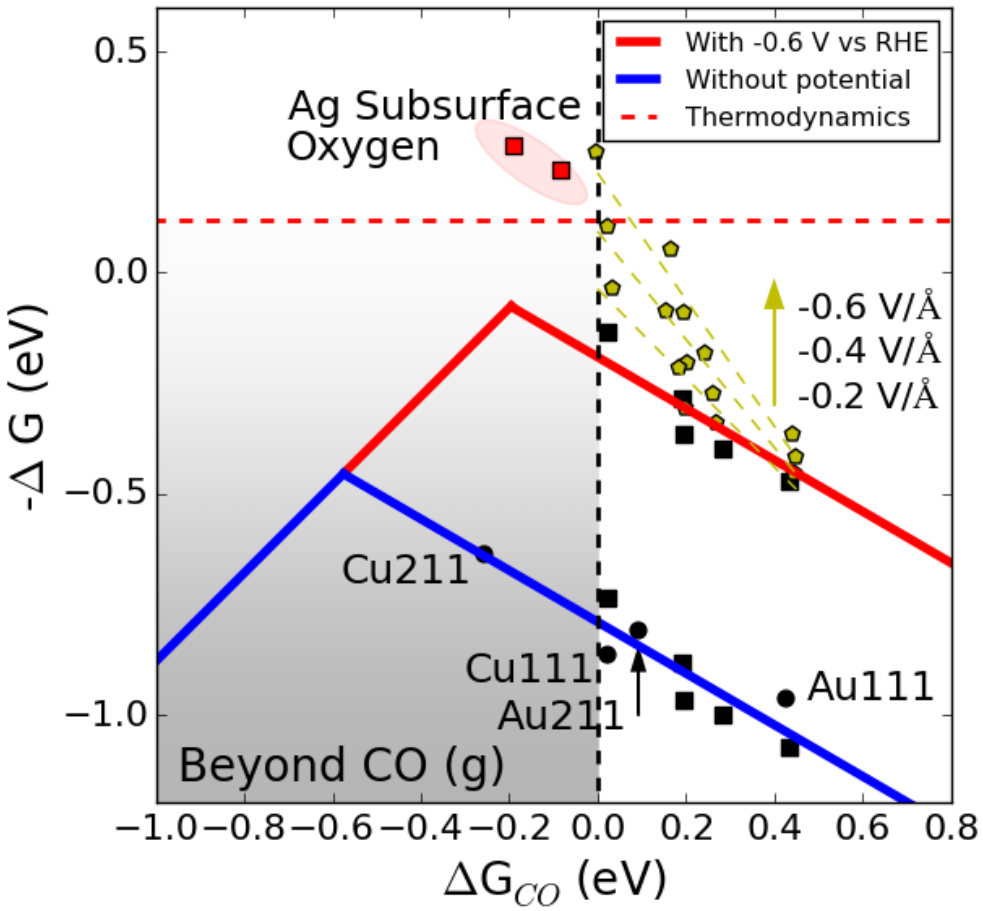

Figure 6. DFT calculated volcano plot of CO_2 reduction to CO. The blue and red lines represent the volcano at 0 and -0.6 V vs. RHE, respectively. The free energy on the weak binding side is defined as the $CO_2 + H^+ + e^- \rightarrow COOH^*$ potential dependent step, which is given as a function of the CO binding energy for 111 and 211 Cu and Au surfaces (black circles) and for multiple defective Ag surfaces (black squares). On the strong binding side, the potential independent reaction $CO^* \rightarrow CO$ step is the limiting factor. Two Ag subsurface oxygen structures have been

included at -0.6 V vs. RHE potential (red squares). The Ag defect sites with applied negative electric field are shown in yellow.

In this study, we demonstrated the highly enhanced activity and CO selectivity of Ag catalysts synthesized through facile plasma treatments. Oxygen plasma treated Ag showed more than 90% Faradaic efficiency towards CO at -0.6 V vs. RHE, a significant improvement over metallic Ag which requires more than -0.9V vs. RHE to reduce CO_2. TEM and *operando* EXAFS showed that although reduction of the oxides occurred during the first 30 min of reaction, oxygen remained in the bulk of the catalyst even after 1 hour of reaction. However, quasi-*in situ* XPS measurements revealed that the near surface region of the catalyst is reduced to metallic Ag under reaction conditions with the first 3 minutes. The mechanism behind the improved reactivity was unraveled by DFT calculations, which indicated that the highly defective surface created by plasma oxidation in the presence of local electric fields can lower the thermodynamic barriers allowing CO_2 reduction to CO at low overpotential. Therefore, our results reveal that a high population of stable defects is critical in creating improved and efficient Ag-based catalysts for CO_2 electroreduction.

Acknowledgement

This work was funded by the German Federal Ministry of Education and Research (Bundesministerium für Bildung und Forschung, BMBF) under grant #03SF0523C - 'CO2EKAT', the Cluster of Excellence RESOLV at RUB (EXC 1069) funded by the Deutsche Forschungsgemeinschaft, and the flagship "Climate KIC/EnCO_2re" program as part of the Horizon2020 EU funding instrument and the Carlsberg Foundation (grant CF15-0165). In addition, financial support was provided by the US National Science Foundation (NSF-CHEM 1213182). Resources of MRCAT at the Advanced Photon Source operated for the US Department of Energy (DOE) by Argonne National Laboratory (ANL) under Contract No. DE-AC02-06CH11357 were used. MRCAT is funded by the MRCAT member institutions and DOE. User support at beamline 10-ID-B was provided by Joshua Wright. The authors gratefully acknowledge the SAMBA beamline at the Soleil synchrotron facility, and user support by Laurent Gautier. C.S.B. and J.C.Y. acknowledge support by NSF-CHE-1534630 and DOE-BES

(DE FG02-03ER15476). Dr. Marco Cordeiro is kindly thanked for his technical support during the EDS acquisition. Transmission electron microscopy work was performed at the Center for Functional Nanomaterials, a DOE Office of Science Facility, at Brookhaven National Laboratory under Contract No. DE-SC0012704.

References

[1] a) E. V. Kondratenko, G. Mul, J. Baltrusaitis, G. O. Larrazábal, J. Pérez-Ramírez, *Energ. Eviron. Sci.* **2013**, *6*, 3112-3135; b) D. T. Whipple, P. J. Kenis, *J. Phys. Chem. Lett.* **2010**, *1*, 3451-3458.

[2] a) H. Mistry, R. Reske, Z. Zeng, Z.-J. Zhao, J. Greeley, P. Strasser, B. R. Cuenya, *J. Am. Chem. Soc.* **2014**, *136*, 16473-16476; b) Y. Hori, A. Murata, K. Kikuchi, S. Suzuki, *J. Chem. Soc., Chem. Commun.* **1987**, 728-729.

[3] T. Hatsukade, K. P. Kuhl, E. R. Cave, D. N. Abram, T. F. Jaramillo, *PCCP* **2014**, *16*, 13814-13819.

[4] a) Q. Lu, J. Rosen, F. Jiao, *ChemCatChem* **2015**, *7*, 38-47; b) C. Kim, H. S. Jeon, T. Eom, M. S. Jee, H. Kim, C. M. Friend, B. K. Min, Y. J. Hwang, *J. Am. Chem. Soc.* **2015**, *137*, 13844-13850; c) A. Salehi-Khojin, H.-R. M. Jhong, B. A. Rosen, W. Zhu, S. Ma, P. J. A. Kenis, R. I. Masel, *J. Phys. Chem. C* **2013**, *117*, 1627-1632; d) C. Kim, T. Eom, M. S. Jee, H. Jung, H. Kim, B. K. Min, Y. J. Hwang, *ACS Catal.* **2017**, *7*, 779-785; e) S. Ma, J. Liu, K. Sasaki, S. Lyth, P. Kenis, *Energy Technology* **2016**, n/a-n/a; f) S. Ma , Y. Lan , G. M. J. Perez, S. Moniri, P. J. A. Kenis *ChemSusChem* **2014**, *7*, 866-874.

[5] a) L. Zhang, Z. Wang, N. Mehio, X. Jin, S. Dai, *ChemSusChem* **2016**; b) Y. Yoon, A. S. Hall, Y. Surendranath, *Angew. Chem.* **2016**, *128*, 15508-15512; c) H. Wang, Z. Han, L. Zhang, C. Cui, X. Zhu, X. Liu, J. Han, Q. Ge, *J. CO2 Util.* **2016**, *15*, 41-49; d) Q. Lu, J. Rosen, Y. Zhou, G. S. Hutchings, Y. C. Kimmel, J. G. Chen, F. Jiao, *Nat. Commun.* **2014**, *5*.

[6] J. Rosen, G. S. Hutchings, Q. Lu, S. Rivera, Y. Zhou, D. G. Vlachos, F. Jiao, *ACS Catal.* **2015**, *5*, 4293-4299.

[7] a) M. Ma, B. J. Trześniewski, J. Xie, W. A. Smith, *Angew. Chem. Int. Ed.* **2016**, *55*, 9748-9752; b) M. S. Jee, H. S. Jeon, C. Kim, H. Lee, J. H. Koh, J. Cho, B. K. Min, Y. J. Hwang, *Appl. Catal. B: Environ.* **2016**, *180*, 372-378; c) M. S. Jee, H. Kim, H. S. Jeon, K. H. Chae, J. Cho, B. K. Min, Y. J. Hwang, *Catal. Today* **2016**; d) Y.-C. Hsieh, S. D. Senanayake, Y. Zhang, W. Xu, D. E. Polyansky, *ACS Catal.* **2015**, *5*, 5349-5356; e) L. Q. Zhou, C. Ling, M. Jones, H. Jia, *Chem. Commun.* **2015**, *51*, 17704-17707.

[8] a) H. Mistry, A. S. Varela, C. S. Bonifacio, I. Zegkinoglou, I. Sinev, Y.-W. Choi, K. Kisslinger, E. A. Stach, J. C. Yang, P. Strasser, B. Roldan Cuenya, *Nat. Commun.* **2016**, *7*, 12123; b) D. Kim, S. Lee, J. D. Ocon, B. Jeong, J. K. Lee, J. Lee, *PCCP* **2015**, *17*, 824-830; c) A. Eilert, F. Cavalca, F. S. Roberts, J. Osterwalder, C. Liu, M. Favaro, E. J. Crumlin, H. Ogasawara, D. Friebel, L. G. Pettersson, A. Nilsson, *J. Phys. Chem. Lett.* **2017**, *8*, 285-290; d) Y. Chen, M. W. Kanan, *J. Am. Chem. Soc.* **2012**, *134*, 1986-1989; e) A. Dutta, A. Kuzume, M. Rahaman, S. Vesztergom, P. Broekmann, *ACS Catal.* **2015**, *5*, 7498-7502; f) C. W. Li, M. W. Kanan, *J. Am. Chem. Soc.* **2012**, *134*, 7231-7234; g) Y. Chen, C. W. Li, M. W. Kanan, *J. Am. Chem. Soc.* **2012**, *134*, 19969-19972.

[9] J. Rossmeisl, J. K. Nørskov, C. D. Taylor, M. J. Janik, M. Neurock, *J. Phys. Chem. B* **2006**, *110*, 21833-21839.

[10] L. D. Chen, M. Urushihara, K. Chan, J. K. Nørskov, *ACS Catal.* **2016**, *6*, 7133-7139.

Table of Contents

Plasma-activation: Silver catalysts activated with an oxygen plasma treatment showed extraordinary improvement for CO_2 electroreduction compared to flat silver surfaces. Electric field effects on the defect-rich plasma treated surface enabled the reduction of CO_2 to CO at low overpotentials.

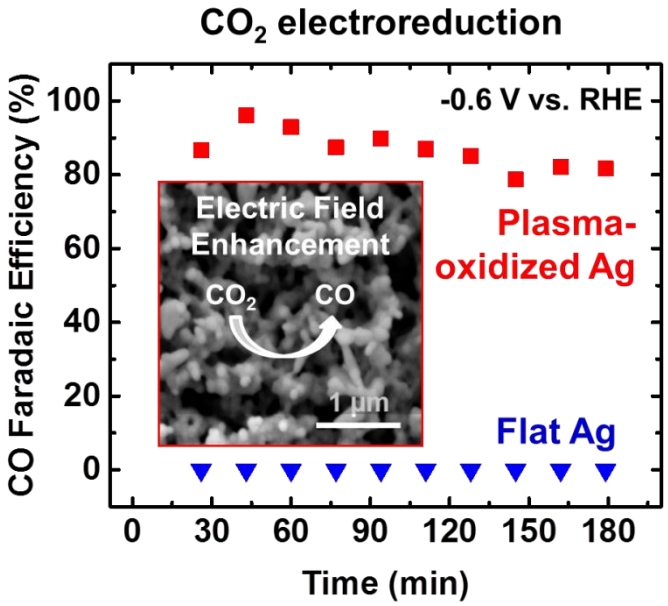

Keywords: silver, electrocatalysis, CO_2 reduction, nanostructure

Supporting Information

Enhanced carbon dioxide electroreduction to carbon monoxide over defect rich plasma-oxidized silver catalysts

Hemma Mistry,[1,2] Yong-Wook Choi,[1] Alexander Bagger,[3] Fabian Scholten,[1] Cecile Bonifacio,[4] Ilya Sinev,[1] Nuria J. Divins,[1] Ioannis Zegkinoglou,[1] Hyo Sang Jeon,[1] Kim Kisslinger,[5] Eric A. Stach,[5] Judith C. Yang,[4] Jan Rossmeisl,[3*] Beatriz Roldan Cuenya[1,*]

[1]Department of Physics, Ruhr University Bochum, 44780 Bochum, Germany

[2]Department of Physics, University of Central Florida, Orlando, Florida 32816, USA

[3]Department of Chemistry, University of Copenhagen, Copenhagen, Denmark

[4]Chemical and Petroleum Engineering and Physics, University of Pittsburgh, Pittsburgh, Pennsylvania 15261, USA.

[5]Center for Functional Nanomaterials, Brookhaven National Laboratory, Upton, New York 11973, USA.

*e-mail: Beatriz.Roldan@rub.de; jan.rossmeisl@chem.ku.dk

Experimental Methods

Synthesis

Ag catalysts were synthesized using 8 µm thick Ag foils, which were plasma treated using either 2 minutes of O_2 plasma, or 10 minutes of H_2 or Ar plasma with 20 W power and a pressure of 400 mtorr. The O_2 + H_2 sample was prepared using 2 minutes of O_2 plasma followed by 10 minutes of H_2 plasma. During the treatment, the samples were laid flat inside the plasma etcher, and after treatment, the back side of the sample was passivated using Kapton tape.

Electron Microscopy

SEM images were acquired using a Quanta 200 FEG microscope from FEI with a field emitter as electron source. A secondary electron (Everhart-Thornley) detector was used for the image acquisition. An electron acceleration voltage of 10 kV and a working distance of 10 mm were used for the measurements.

Cross-section TEM specimens were prepared using a FEI Helios 600 and a FEI Scios dual beam focused ion beam (DB-FIB) at the Center for Functional Nanomaterials (CFN), Brookhaven National Laboratory (BNL) and Nanoscale Fabrication and Characterization Facility (NFCF), University of Pittsburgh, respectively. FIB cross section samples were prepared using 30 KeV with final polishing at 5 KeV. Spatially resolved energy dispersive X-ray spectrometer (EDS) elemental maps of the Ag foils were acquired using a FEI Talos F200X field emission gun (FEG) TEM/STEM at the Center for Functional Nanomaterials, BNL operated at 200 kV equipped with a four-quadrant 0.9-sr EDS.

X-ray Photoelectron Spectroscopy

XPS measurements were performed quasi-*in situ* using an electrochemical cell connected to an ultra-high vacuum (UHV) system. Figure S1 shows the experimental setup used. The glass chamber filled with pressurized argon atmosphere protects the sample from air exposure during the transfer towards the XPS system. The XPS measurements were performed using a Phoibos 100 (SPECS GmbH) analyzer with a pass energy, E_{pass} = 13 eV, and the Al anode of a XR 50 (SPECS GmbH) X-ray source (P_{source} = 300 W).

X-ray Absorption Spectroscopy

X-ray absorption spectroscopy was measured at beamline 10-ID-B of the Advanced Photon Source (APS) at Argonne National Laboratory (Chicago) and at the SAMBA beamline at SOLEIL (Paris). A homebuilt, three-electrode electrochemical cell was used with a Pt counter electrode and leak-free Ag/AgCl reference electrode. The plasma treated silver foils were measured in fluorescence geometry at grazing angle behind a 1 mm electrolyte layer. *Operando* EXAFS of the O_2 and Ar plasma treated samples were performed at APS with a Lytle detector. Each scan took approximately 5 minutes to acquire in continuous motor mode, and spectra which were distorted by bubble formation (from CO_2 bubbling or the reaction products) in front of the sample were discarded. *Operando* EXAFS of the O_2 + H_2 plasma Ag sample were acquired at SOLEIL with a 35 element Ge detector, and each scan took 3 minutes. Data alignment and background removal were performed using the Athena software, and EXAFS fitting was performed using the Artemis software.[1] Theoretical EXAFS were generated using the FEFF8 code.[2]

Electrochemical Characterization

CO_2 reduction was carried out in a customized H-type cell separated by a Nafion ® 115 membrane with 0.1 M $KHCO_3$ (Sigma-Aldrich, ACS reagent, 99.7%). A conventional three-electrode system was used for CO_2 reduction at room temperature with an AutoLab PGSTAT128N potentiostat. A platinum mesh and leak-free Ag/AgCl electrode (LF-1, Innovative Instruments, Inc.) were employed as counter electrode and reference electrode, respectively. Electrolytes were purged with CO_2 gas (99.95%) for 30 min until a pH of 6.8 was reached before the electrochemical measurements. During CO_2 electrolysis, chronoamperometry was used to reduce CO_2 at -0.6 V vs RHE for 3 h by maintaining constant CO_2 flow rate as 20 mL/min with vigorous stirring (1100 rpm). The gas phase products were injected into a gas chromatograph (Agilent 7890A online system) every 17 min during CO_2 electrolysis for detection of products. High-performance liquid chromatography (HPLC, Shimadzu) was used to check for the presence of minor liquid products such as formate and alcohols during CO_2 reduction at -0.6 V vs RHE. To gain insight into the electrochemical surface area or film roughness, the double layer capacitance was measured after 1 hour and 3 hours of reaction in 0.1 M $HClO_4$ (VWR chemicals, ACS reagent, 69.6%) between 0.3V and 0.4 V vs. RHE with several scan rates.

DFT calculations

The Cu, Au and Ag structures were created in ASE[3], and models of the structures for the Ag defects are shown in Figure S11 right, together with a unit cell of the Ag_2O with surface oxygens removed. For the 111 facet, 111 adatom and 211 step (4×4×1) k-points were used, and for the 211 kink and 211 adatom, (4×2×1) k-points were used. For the electronic structure calculations the projector augmented wave method[4] and the revised Perdew-Burke-Ernzerhof (RPBE)[5] functional was performed with the GPAW software.[6] Furthermore, a 0.17 grid spacing was used and all the structures were relaxed to a force below 0.05 eV/Å. To calculate the free energy diagrams, the computational hydrogen electrode was employed.[7] For thermodynamic values, the values from reference [8] were used, and the CO_2 calculated RPBE energy was corrected by 0.45 eV together with a –COH and CO* water correction of 0.25 and 0.1 eV[9], respectively, to account for known systematic errors in their energies.

Additional Discussion

iR Compensation

In order to reduce the error between measurements in the operando electrochemical cell and the H-type cell used for reactivity measurements due to their different geometries, iR compensation was carried out through electrochemical impedance spectroscopy (EIS). We checked the uncompensated resistance (R_u) in our H-type cell and operando electrochemical cell, as shown in Figure S16. To calculate iR values, the value of the current is derived from Figure S17 measured via linear sweep voltammetry (LSV), and calculated values are shown in Table S4 by using 85% of R_u.[10] Therefore, the difference in the real potential value in the different cell systems can be considered negligible. Vigorous stirring of the electrolyte was not performed during measurements in the operando cell, which can explain why the current signal of the operando cell is lower than the H-type cell.

DFT of Ag Subsurface Oxygen Models

DFT was used to investigate the possible effects of subsurface oxygen on the reaction using two structures: An Ag 111 facet with subsurface oxygen and an Ag_2O 111 facet with surface oxygen atoms removed, labelled in Figure 6 as “Ag Subsurface Oxygen” (red squares at -

0.6 V vs. RHE). However, the Ag subsurface oxygen models are discarded due to three deviations as compared to the experiments: 1) the subsurface oxygen is highly unstable under reducing conditions, which is in agreement with the XPS results; 2) the subsurface oxygen structures bind CO* strong enough to enable further reduction beyond CO, which is seen in the subsurface data points lying to the left of the dashed black line in Figure 6. The CO* protonation step to CHO* is shown in Figure S12 for both structures, and the further reduction of CO should be possible at the overpotential used in our experiment. However, products beyond CO are not observed in the experiments. 3) HER should be enhanced by the subsurface oxygen in a similar way as the CO_2 reduction reaction (see Figure S13 for HER), since H* binds to the ontop site opposite of the oxygen and thus scales nicely with COOH*.[11] However, the HER in the oxygen plasma samples is limited in the initial/early phase of the experiment where a higher content of oxygen in the samples is expected, which could be due to the effect of reducing oxygen. Due to these three points, it is unlikely that oxygen-deficient silver oxide or subsurface oxygen is responsible for the high performance of our plasma-oxidized Ag catalysts.

Comparison with Other Studies

Recently, much attention has been paid to metal catalysts which are pre-oxidized and then reduced *in situ* under CO_2 electroreduction conditions. These catalysts have been shown to have vastly improved current density and selectivity in comparison to unoxidized catalysts.[12] For certain systems such as oxide-derived copper[12d, 13] or tin,[12c, 14] cationic metal species, oxides, or subsurface oxygen which survive in the catalyst during the reaction have been suggested to play a key role in their improved reactivity. However, oxidation of a metal surface can also cause severe roughening and nanostructuring, as well as an increase in the fraction of low coordinated sites at grain boundaries,[15] each of which may also influence the catalytic reactivity. In a previous study from our group, plasma oxidized copper films were shown to have highly improved production of CO and C_2H_4 and suppression of CH_4 in comparison to untreated Cu. While improvements in current density and partial suppression of CH_4 were related to the surface roughness caused by O_2 plasma, we proved that oxygen species which survive in the catalyst were responsible for lowering the overpotential for CO and C_2H_4. The lack of one-to-one correlation between the surface roughness and the reaction selectivity was demonstrated by comparing the selectivity of two samples initially pre-treated with O_2-plasma but one of them

subsequently exposed to a final H_2 plasma treatment. In that case, both samples ended up with analogous surface roughness, but only the one which was not exposed to atomic H displayed high selectivity for C-C coupling (C_2H_4 production) vs. CH_4. Our results on oxidized Cu foils are in contrast to those found here for plasma-oxidized Ag, in which no oxygen survives in the sample surface under reaction conditions (XPS), and the high population of defects on the sample surface was found to enhance the reactivity. One key different between the two metals is that Cu interacts much more strongly with oxygen and forms oxides more readily than Ag. Therefore, under reaction conditions, Ag may not stabilize any near surface oxygen, as demonstrated by our quasi-in situ XPS, while Cu can.

Plasma-oxidation of Ag films is shown here to be a facile method to synthesize rough and defective surfaces which are highly efficient for CO_2 electroreduction and low overpotential. Other studies have also investigated oxidized Ag films for CO_2 reduction, which were synthesized using electrochemical methods.[16] In comparison to those studies, our plasma-oxidized Ag shows lower overpotential and much higher current density for CO than those synthesized electrochemically. This is likely due to the highly facile oxidation of Ag with atomic oxygen during the plasma treatment, which results in a much thicker oxide layer, rougher surface structure, and a higher defect density. Although some studies proposed that surface oxygen species may be stable on oxidized Ag during the reaction,[16b, 17] ours is the first quasi-*in situ* study showing that in fact the surface of oxide-derived Ag is quickly reduced (within the first 3 minutes) under reaction conditions, Figure 4c.

Another mechanism that has been proposed to improve the reactivity of nanostructured Ag is mass transport effects in a highly porous mesostructured surface. Recently, Yoon et al. have shown that increasing the porosity of Ag catalysts for CO_2 reduction can suppress HER while simultaneously enhancing CO_2 reduction, due to the inhibited mass transfer on the mesostructured catalysts.[18] Although mass transfer effects may play a role in enhancing the activity of our oxidized Ag, our more porous catalysts do not show a corresponding suppression of HER. Lu et al. have also investigated nanoporous Ag as an improved catalyst for CO_2 electroreduction, finding higher CO currents at -0.6 V vs. RHE.[19] Since the catalysts in their study were synthesized from the dealloying of Ag-Al, it may be possible that Al dopants remain in the catalyst, which may enhance the reactivity for CO_2 reduction. Using DFT, Lim et al. have

shown that p-block dopants such as Al can lower the overpotential of CO_2 electroreduction on Ag by around -0.5 V.[20]

Our results provide a comprehensive picture of the role of O_2-plasma treatments in the generation of defects that may act as activate sites in catalytic reactions. While the plasma-generated oxides or subsurface oxygen may remain in the bulk of our Ag catalyst during the CO_2 electrochemical reaction, the near surface region of the catalyst is reduced under reaction conditions, indicating that the active component is a roughened and highly defective metallic Ag surface. According to our DFT results, the defective metallic Ag sites in the presence of local electric fields allow low overpotential reduction of CO_2 to CO. In comparison, more closed packed Ag surfaces with few defects cannot reduce CO_2 at low overpotential. These results contrast with oxide-derived Cu catalyst for CO_2 reduction, which have been shown to contain subsurface oxygen or oxides near/at the surface during the reaction which enhance their reactivity.[12d, 13a, 13b] However, silver has a much lower affinity for oxygen than copper, which could explain why the surface of the silver catalysts is more easily reduced during this reaction.

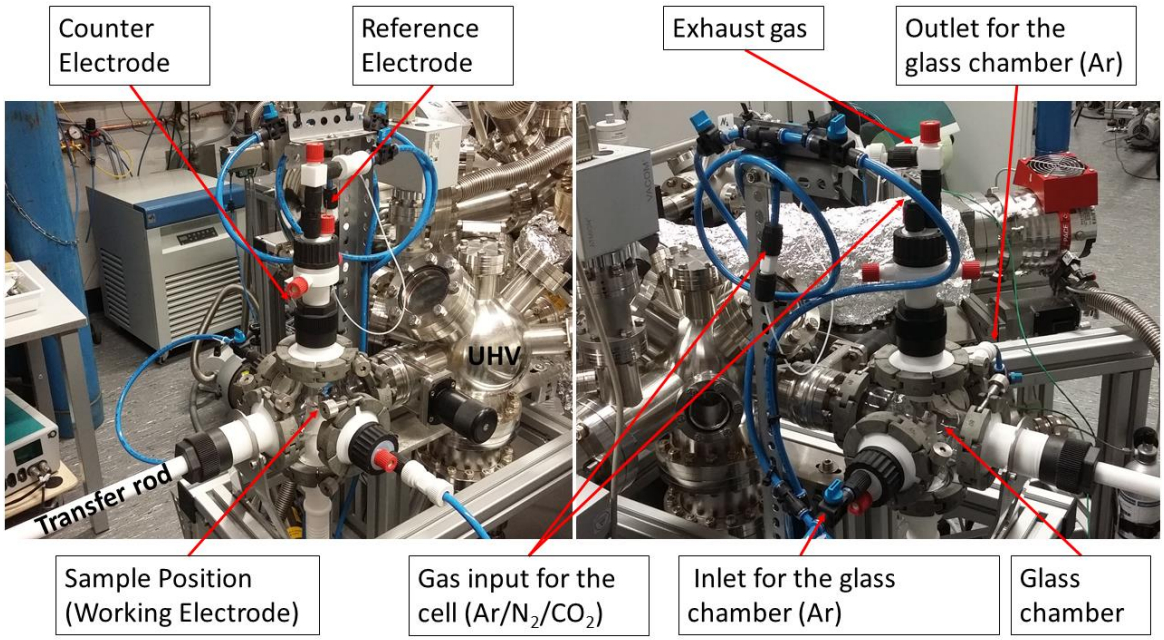

Figure S1. Electrochemical cell (white) connected to the used UHV system via a glass chamber filled with pressurized argon gas atmosphere to protect the samples upon exposure to air.

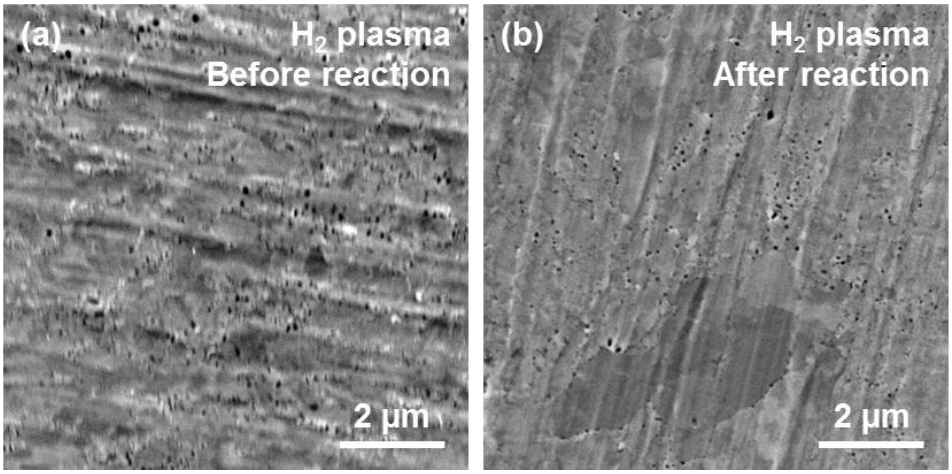

Figure S2. SEM images of H_2 plasma treated Ag foil (a) as prepared and (b) after 1 hour of CO_2 electroreduction at -0.6 V vs. RHE.

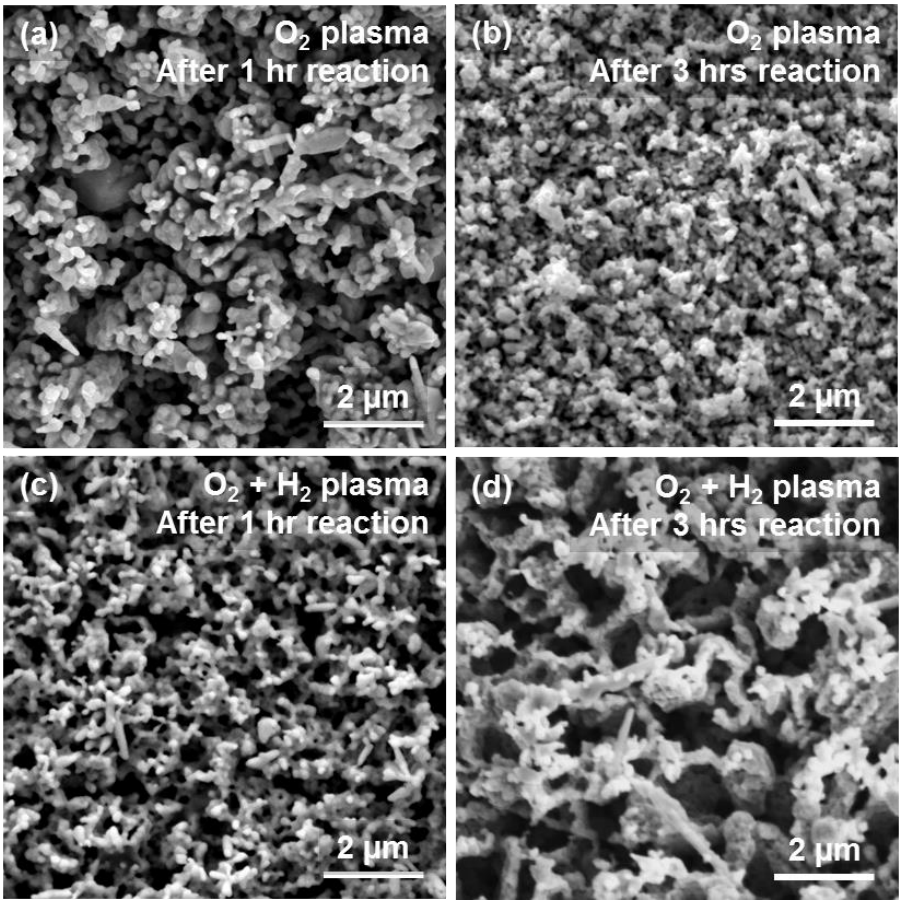

Figure S3. SEM images of O_2 plasma and O_2 + H_2 plasma treated Ag foil (a,c) after 1 hour of reaction at -0.6 V vs. RHE and (b,d) after 3 hours of CO_2 electroreduction at -0.6 V vs. RHE.

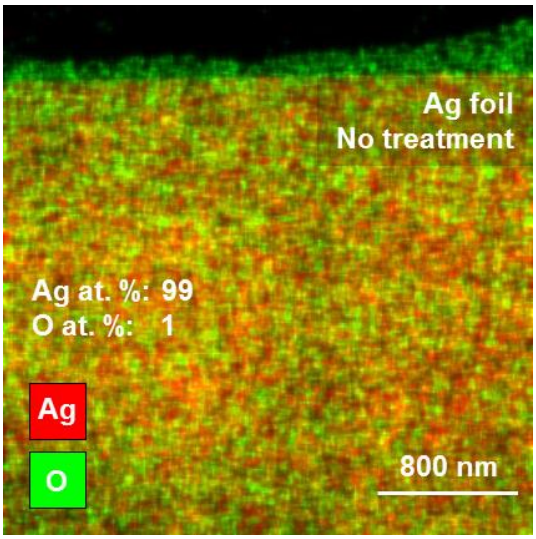

Figure S4. STEM-EDS maps of the Ag foil cross-section with no plasma treatment. Minimal oxidation of the sample occurs during the preparation of cross-sections for TEM, which is to be expected since Ag does not readily form oxides in air at room temperature.[21]

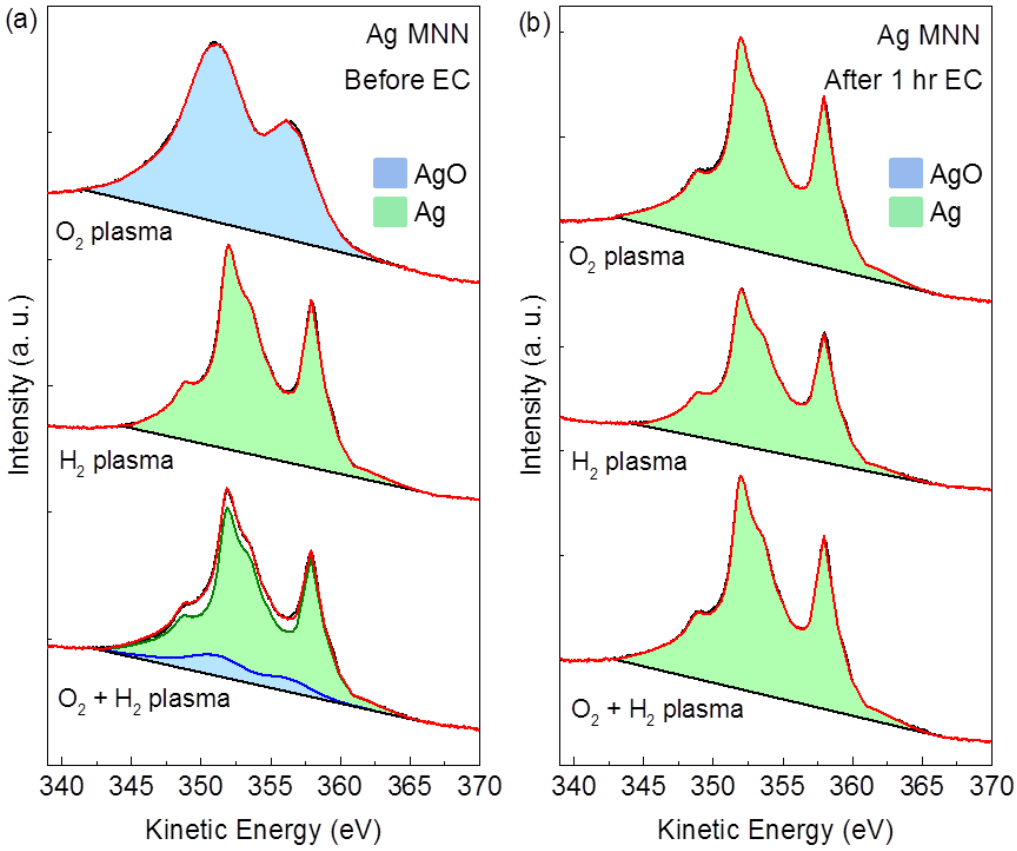

Figure S5. XPS measurements of the Ag MNN Auger region of O_2, H_2 and O_2+H_2 plasma treated Ag catalysts (a) as prepared and (b) after 1 hour of CO_2 electroreduction at -0.6 V vs. RHE and UHV transfer to XPS.

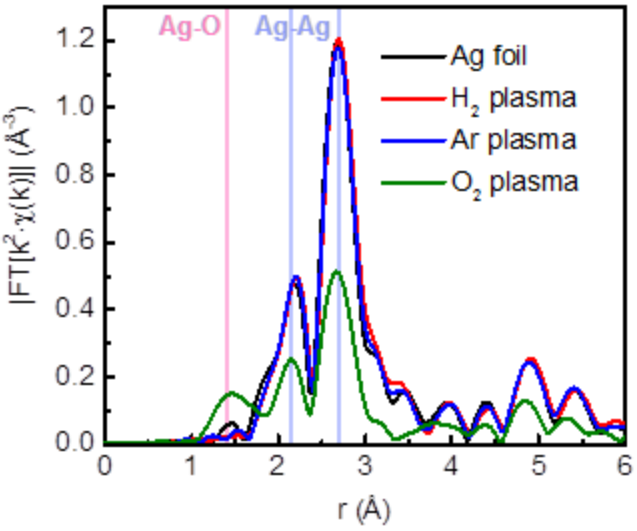

Figure S6. Ag K-edge k^2-weighted EXAFS of Ag foils measured in air after various plasma treatments. An untreated Ag foil is also plotted for reference

Table S1. EXAFS fitting results, including first nearest neighbor coordination number (N), bond length (r), and disorder parameter (σ^2) for as prepared plasma-treated Ag foils treated with O_2 and H_2 plasmas for various times measured in air at the Ag K-edge.

	Ag-Ag			Ag-O		
	N	**r (Å)**	**σ^2 (Å^2)**	**N**	**r (Å)**	**σ^2 (Å^2)**
Ag foil	12	2.861 ± 0.004	0.0099 ± 0.005	-	-	-
H_2 plasma	12.3 ± 0.7	2.862 ± 0.003	0.0101 ± 0.0005	-	-	-
Ar plasma	11.9 ± 0.7	2.862 ± 0.004	0.0099 ± 0.005	-	-	-
O_2 plasma	4.8 ± 0.4	2.861 ± 0.004	0.0088 ± 0.0006	0.6 ± 0.2	2.02 ± 0.01	0.002 ± 0.003

Table S2. EXAFS fitting results, including first nearest neighbor coordination number (N), bond length (r), and disorder parameter (σ^2) for plasma-treated Ag foils measured in air and *operando* over time at the Ag K-edge. Spectra are shown in Figure 3.

Sample /Treatment	**Ag-Ag**			**Ag-O**		
	N	**r (Å)**	**σ^2 (Å^2)**	**N**	**r (Å)**	**σ^2 (Å^2)**
O_2 plasma Air	4.8 ± 0.4	2.861 ± 0.004	0.0088 ± 0.0006	0.6 ± 0.2	2.02 ± 0.01	0.002 ± 0.003
15 min	5.3 ± 0.5	2.863 ± 0.006	0.0099 ± 0.0009	0.5 ± 0.3	1.91 ± 0.04	0.000 ± 0.005
30 min	6.6 ± 0.4	2.854 ± 0.004	0.0096 ± 0.0005	0.5 ± 0.5	2.04 ± 0.04	0.01 ± 0.02
35 min	9.2 ± 0.8	2.866 ± 0.005	0.0090 ± 0.0006	-	-	-
65 min	11 ± 1	2.863 ± 0.006	0.0105 ± 0.0008	-	-	-
Ag foil	12	2.861 ± 0.004	0.0099 ± 0.005	-	-	-
O_2 + H_2 plasma Air	6.5 ± 0.4	2.862 ± 0.003	0.0091 ± 0.0005	0.3 ± 0.1	2.08 ± 0.03	0.000 ± 0.004
3 min	9 ± 1	2.850 ± 0.008	0.009 ± 0.002	-	-	-
15 min	11 ± 1	2.860 ± 0.004	0.0102 ± 0.0008	-	-	-
24 min	11 ± 1	2.868 ± 0.005	0.009 ± 0.001	-	-	-
60 min	10.9 ± 0.7	2.869 ± 0.004	0.0096 ± 0.0007	-	-	-

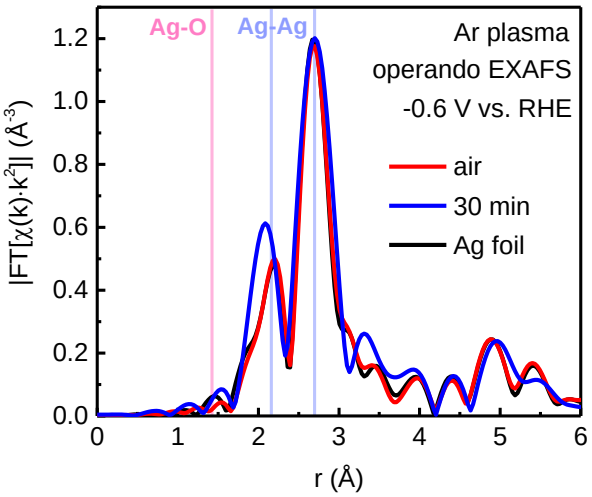

Figure S7. Ag K-edge k^2-weighted EXAFS of Ar plasma treated Ag measured in air and *operando* at 30 minutes of CO_2 electroreduction in 0.1M $KHCO_3$ at -0.6 V vs. RHE. The spectra are similar in structure to an untreated metallic Ag foil (also plotted for reference) and no changes could be detected over 30 minutes of reaction.

Table S3. EXAFS fitting results, including first nearest neighbor coordination number (N), bond length (r), and disorder parameter (σ^2) for Ag foils treated with Ar plasma measured in air and operando after 30 minutes at the Ag K-edge.

	Ag-Ag			Ag-O		
	N	**r (Å)**	**σ^2 (Å^2)**	**N**	**r (Å)**	**σ^2 (Å^2)**
air	11.9 ± 0.7	2.862 ± 0.004	0.0099 ± 0.005	-	-	-
30 min	12 ± 1	2.853 ± 0.005	0.0083 ± 0.0008	-	-	-
Ag foil	12	2.861 ± 0.004	0.0099 ± 0.005	-	-	-

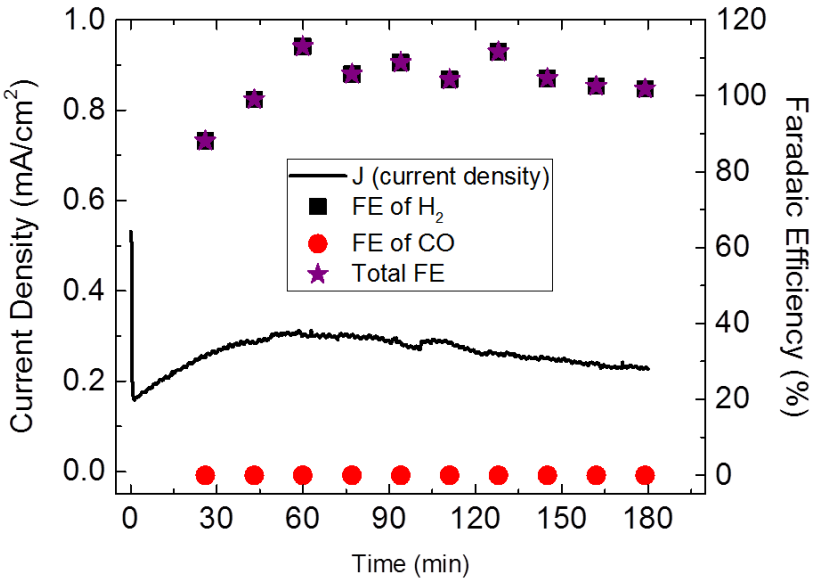

Figure S8. Current density and faradaic efficiency of an untreated Ag foil during CO_2 electroreduction at -0.6 V vs. RHE.

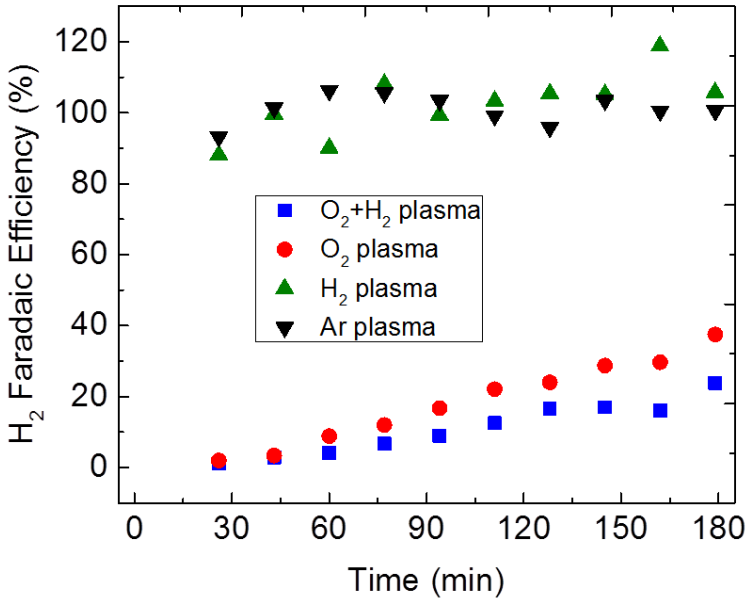

Figure S9. Faradaic efficiency for H_2 for all samples at -0.6V vs. RHE during CO_2 electroreduction in 0.1 M $KHCO_3$.

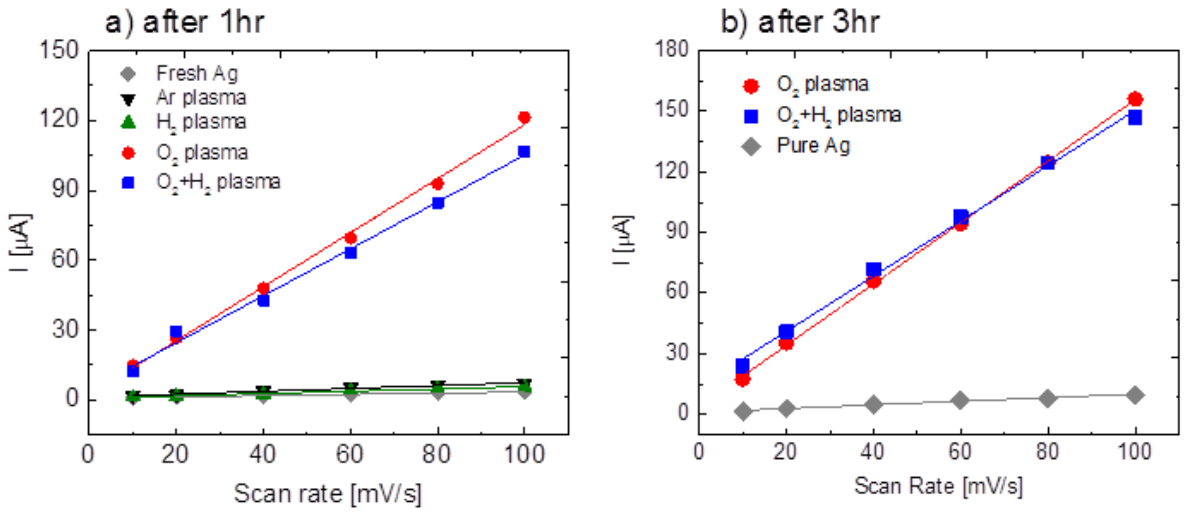

Figure S10. Roughness factor measurements by cyclic voltammetry (CV) in the potential region between +0.3 and +0.4 V vs RHE with the catalysts after 1 hour or 3 hours of CO_2 reduction under 0.1M $HClO_4$. The points indicate the amount of double layer charging and discharging at every scan rate (10, 20, 40, 60, 80 and 100 mV/s).

Table S4. The surface roughness factor after 1 hour of reaction determined by the slopes of the total charge vs. CV scan rate. The surface roughness factors are calculated by normalizing the slopes in Fig. S6 by the fresh Ag foil, which is defined to have a roughness factor of 1. The roughness factors of the pre-oxidized foils were also measured after 3 hours of reaction.

	Roughness Factor	
Sample	**1 hour**	**3 hours**
O_2+H_2 plasma	34	15
O_2 plasma	39	17
H_2 plasma	1.7	-
Ar plasma	2.0	-
Fresh Ag	1.0	1.0

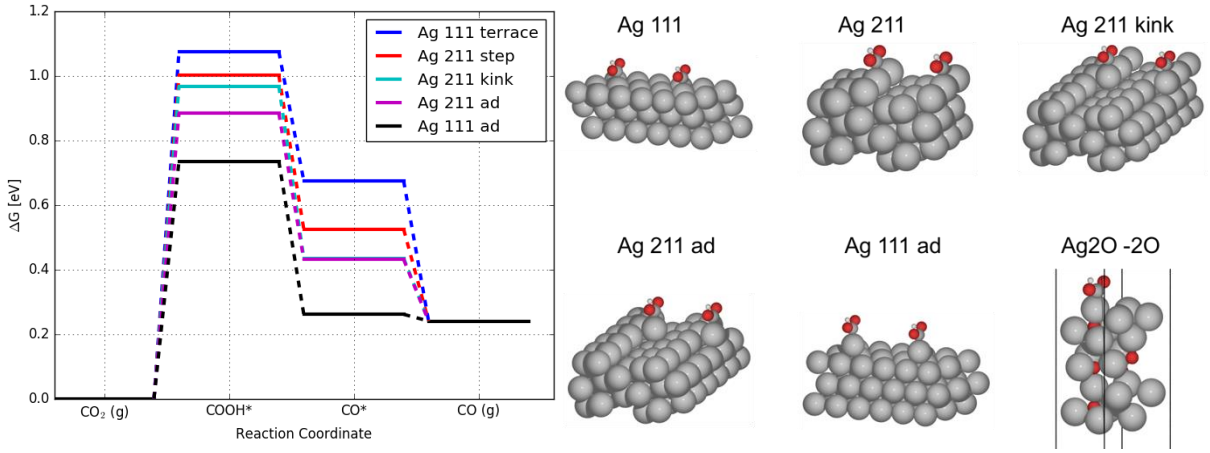

Figure S11. Left: Free energy diagram of CO_2 to CO on Ag defects. Right: Ag defect structures (repeated in x-direction) and the Ag_2O oxide structure, which is a Ag_2O 111 surface where two surface oxygen atoms have been removed, giving only a subsurface oxygen for the oxide.

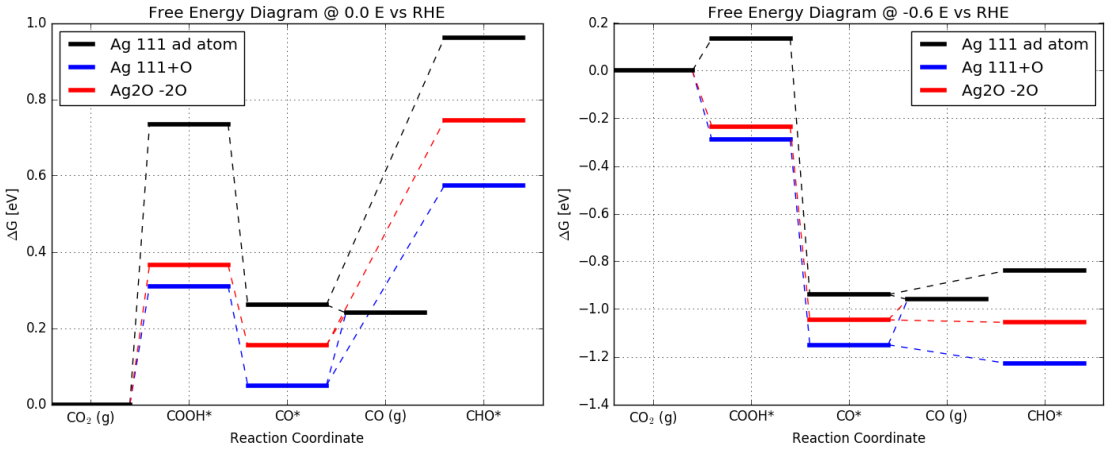

Figure S12. Free energy diagram of CO_2 (g) reduction to CO (g) and CHO* on Ag 111 adatom, Ag 111 with subsurface oxygen and Ag_2O 111 facet with the surface oxygens removed. Left: The free energy diagram at 0 V vs. RHE potential. Right: the free energy diagram with a -0.6 V vs. RHE potential used, similar to the experiments.

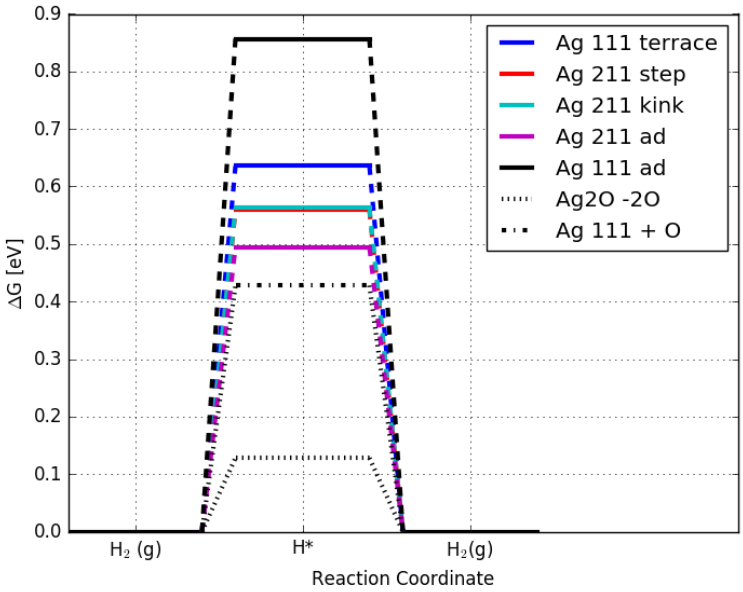

Figure S13. Free energy diagram of the Hydrogen Evolution Reaction (HER) on the Ag defects and the Ag subsurface structures.

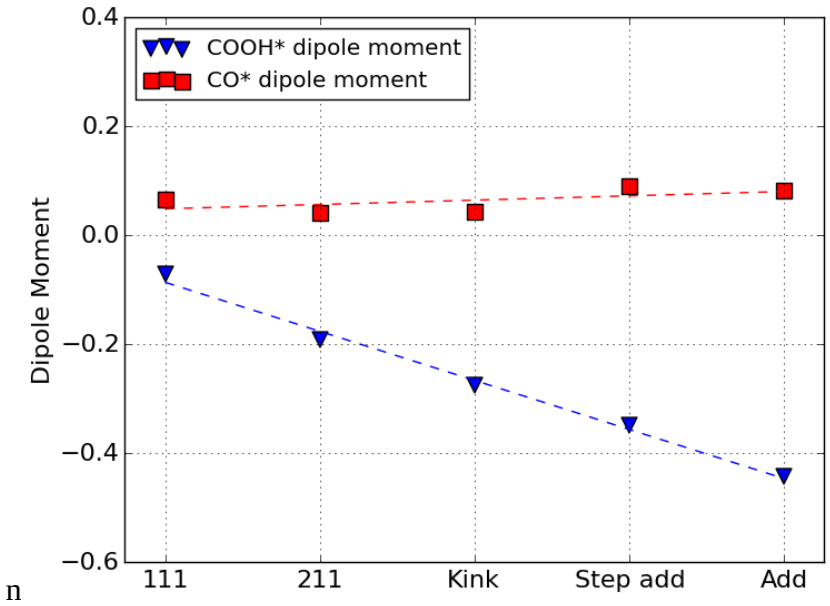

n

Figure S14. The dipole moment orthogonal to each surface for the COOH* and CO* adsorbate on the Ag defects. The Dipole Moment (DM) of the adsorbates are calculated as DM = $DM_{COOH+Slab}$-DM_{Slab}.

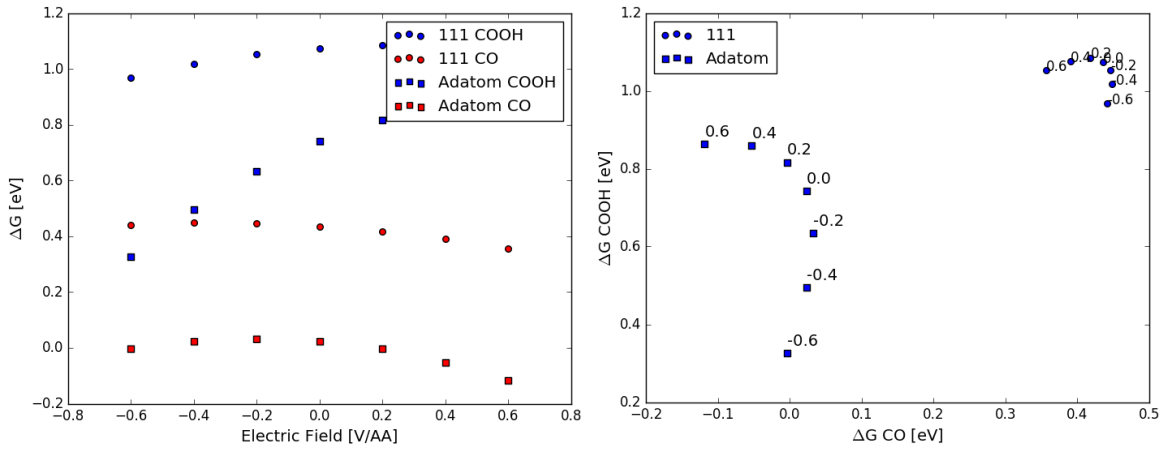

Figure S15. Electric field calculations for the Ag 111 facet and the Ag 111 adatom. Left: The COOH* and CO* adsorbates as a function of electric field. Right: The COOH* free energy vs. the CO* free energy at different fields written within the plot. The COOH* adsorbate depends on the negative electric fields and little on the positive electric fields, while the CO* adsorbate depends on positive electric field and little on negative electric fields.

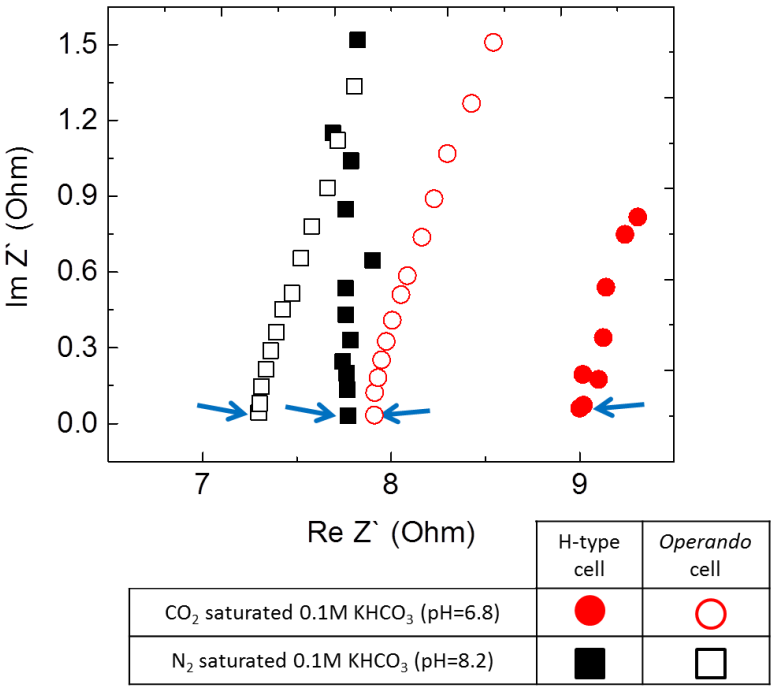

Figure S16. EIS signals in the operando electrochemical cell (open symbols) and H-type electrochemical cell (solid symbols) in CO_2 (red) and N_2 (black) saturated electrolyte. EIS experiments carried out in the frequency range of 10 kHz to 100 mHz at -0.6 V vs RHE. Blue arrows indicate the points of uncompensated resistance. Measurements were performed using an O_2 plasma treated Ag foil as working electrode.

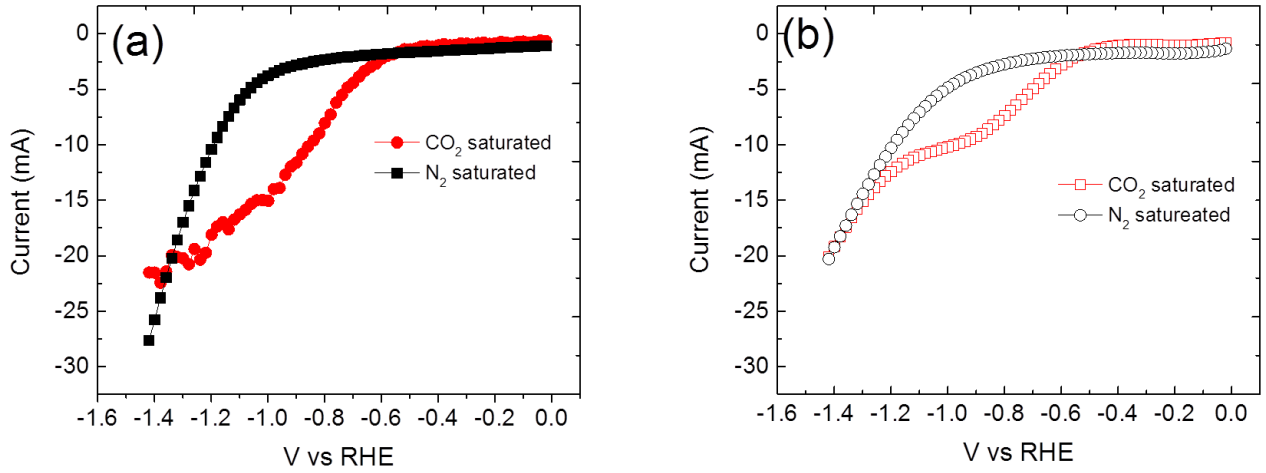

Figure S17. LSV curves measured in the H-type cell (a) and operando cell (b). Sweep speed is 50 mV/s and the voltage range is from 0 V vs. RHE to -1.4 V vs. RHE with CO_2 saturated 0.1 M $KHCO_3$ (red circles) and N_2 saturated 0.1 M $KHCO_3$ (black squares).

Table S5. The values of compensated iR derived by multiplying 85% of R_u and the value of current derived from Figure S17.

Cell type	Saturated gas type in 0.1 M $KHCO_3$	Uncompensated resistance (R_u) [ohm]		Current [mA] at -0.6 V vs RHE	iR value [mV]
		Measured (100%)	85% R_u		
H-type	CO_2	9	7.7	2.3	17.7
	N_2	7.8	6.6	1.9	12.5
Operando	CO_2	7.9	6.7	2.8	18.8
	N_2	7.3	6.2	2	12.4

References

[1] M. Newville, *J. Synchrotron Radiat.* **2001**, *8*, 322-324.

[2] A. Ankudinov, B. Ravel, J. Rehr, S. Conradson, *Phys. Rev. B* **1998**, *58*, 7565.

[3] S. R. Bahn, K. W. Jacobsen, *Computing in Science & Engineering* **2002**, *4*, 56-66.

[4] P. E. Blöchl, *Phys. Rev. B* **1994**, *50*, 17953-17979.

[5] B. Hammer, L. B. Hansen, J. K. Nørskov, *Phys. Rev. B* **1999**, *59*, 7413-7421.

[6] a) J. J. Mortensen, L. B. Hansen, K. W. Jacobsen, *Phys. Rev. B* **2005**, *71*, 035109; b) J. Enkovaara, C. Rostgaard, J. J. Mortensen, J. Chen, M. Dułak, L. Ferrighi, J. Gavnholt, C. Glinsvad, V. Haikola, H. A. Hansen, H. H. Kristoffersen, M. Kuisma, A. H. Larsen, L. Lehtovaara, M. Ljungberg, O. Lopez-Acevedo, P. G. Moses, J. Ojanen, T. Olsen, V. Petzold, N. A. Romero, J. Stausholm-Møller, M. Strange, G. A. Tritsaris, M. Vanin, M. Walter, B. Hammer, H. Häkkinen, G. K. H. Madsen, R. M. Nieminen, J. K. Nørskov, M. Puska, T. T. Rantala, J. Schiøtz, K. S. Thygesen, K. W. Jacobsen, *J. Phys.: Condens. Matter* **2010**, *22*, 253202.

[7] J. K. Nørskov, J. Rossmeisl, A. Logadottir, L. Lindqvist, J. R. Kitchin, T. Bligaard, H. Jónsson, *J. Phys. Chem. B* **2004**, *108*, 17886-17892.

[8] K. Chan, C. Tsai, H. A. Hansen, J. K. Nørskov, *ChemCatChem* **2014**, *6*, 1899-1905.

[9] A. A. Peterson, F. Abild-Pedersen, F. Studt, J. Rossmeisl, J. K. Nørskov, *Energ. Eviron. Sci.* **2010**, *3*, 1311-1315.

[10] K. P. Kuhl, E. R. Cave, D. N. Abram, T. F. Jaramillo, *Energ. Eviron. Sci.* **2012**, *5*, 7050-7059.

[11] A. Bagger, W. Ju, A. S. Varela, P. Strasser, J. Rossmeisl, *Catal. Today* **2017**.

[12] a) C. W. Li, M. W. Kanan, *J. Am. Chem. Soc.* **2012**, *134*, 7231-7234; b) Y. Chen, C. W. Li, M. W. Kanan, *J. Am. Chem. Soc.* **2012**, *134*, 19969-19972; c) Y. Chen, M. W. Kanan, *J. Am. Chem. Soc.* **2012**, *134*, 1986-1989; d) H. Mistry, A. S. Varela, C. S. Bonifacio, I. Zegkinoglou, I. Sinev, Y.-W. Choi, K. Kisslinger, E. A. Stach, J. C. Yang, P. Strasser, B. Roldan Cuenya, *Nat. Commun.* **2016**, *7*, 12123.

[13] a) D. Kim, S. Lee, J. D. Ocon, B. Jeong, J. K. Lee, J. Lee, *PCCP* **2015**, *17*, 824-830; b) A. Eilert, F. Cavalca, F. S. Roberts, J. Osterwalder, C. Liu, M. Favaro, E. J. Crumlin, H. Ogasawara, D. Friebel, L. G. Pettersson, A. Nilsson, *J. Phys. Chem. Lett.* **2017**, *8*, 285-290; c) D. Gao, I. Zegkinoglou, N. J. Divins, F. Scholten, I. Sinev, P. Grosse, B. Roldan Cuenya, *ACS Nano* **2017**, *11*, 4825-4831.

[14] A. Dutta, A. Kuzume, M. Rahaman, S. Vesztergom, P. Broekmann, *ACS Catal.* **2015**, *5*, 7498-7502.

[15] a) X. Feng, K. Jiang, S. Fan, M. W. Kanan, *J. Am. Chem. Soc.* **2015**, *137*, 4606-4609; b) A. Verdaguer-Casadevall, C. W. Li, T. P. Johansson, S. B. Scott, J. T. McKeown, M. Kumar, I. E. Stephens, M. W. Kanan, I. Chorkendorff, *J. Am. Chem. Soc.* **2015**, *137*, 9808-9811.

[16] a) M. Ma, B. J. Trześniewski, J. Xie, W. A. Smith, *Angew. Chem. Int. Ed.* **2016**, *55*, 9748-9752; b) M. S. Jee, H. S. Jeon, C. Kim, H. Lee, J. H. Koh, J. Cho, B. K. Min, Y. J. Hwang, *Appl. Catal. B: Environ.* **2016**, *180*, 372-378.

[17] M. S. Jee, H. Kim, H. S. Jeon, K. H. Chae, J. Cho, B. K. Min, Y. J. Hwang, *Catal. Today* **2016**.

[18] Y. Yoon, A. S. Hall, Y. Surendranath, *Angew. Chem.* **2016**, *128*, 15508-15512.

[19] Q. Lu, J. Rosen, Y. Zhou, G. S. Hutchings, Y. C. Kimmel, J. G. Chen, F. Jiao, *Nat. Commun.* **2014**, *5*.

[20] H.-K. Lim, H. Shin, W. A. Goddard III, Y. J. Hwang, B. K. Min, H. Kim, *J. Am. Chem. Soc.* **2014**, *136*, 11355-11361.
[21] C. Rehren, M. Muhler, X. Bao, R. Schlögl, G. Ertl, *Z. Phys. Chem.* **1991**, *174*, 11-52.